Journal of Manufacturing Processes 79 (2022) 142–153

Contents lists available at ScienceDirect

Journal of Manufacturing Processes

journal homepage: www.elsevier.com/locate/manpro

A control strategy for incremental profile forming

Ryo Nakahata [a], Satyanarayana Seetharaman [a], Krishnaswamy Srinivasan [a,*], A. Erman Tekkaya [b]

[a] Dept. of Mechanical and Aerospace Engineering, The Ohio State University, Columbus, OH 43210, USA
[b] Institute of Forming Technology and Lightweight Components, TU Dortmund, 44227 Dortmund, Germany

ARTICLE INFO

Keywords:
Incremental forming
Radial indentation
Axial grooving
Material springback
Optical sensing
Control-oriented modelling

ABSTRACT

Incremental profile forming (IPF) allows the flexible manufacture of metallic tubular structures with cross-sectional profiles that vary along their length, but its geometric accuracy is limited currently by exclusive reliance upon machine control of the process. Procedures for on-line sensing of process attributes and post-process sensing of part geometry, using laser triangulation sensors, are developed. Improved understanding of process characteristics for elementary IPF operations, obtained from FEM analysis and experiments, is described. Issues in developing a control-oriented process model are discussed along with prior related work. An overall control strategy for improving part geometry in IPF is formulated, indicating directions for needed research in process design, control-oriented modelling, sensing improvements, and control.

1. Motivation and introduction

Incremental Profile Forming (IPF) belongs to a group of methods for profile manufacturing that have been developed in recent years for small and medium lot production of complex load-adapted structures to meet the needs of resource efficiency and weight reduction. Beside process flexibility, increased part geometric complexity is required for such structures. While conventional tube forming processes have been enhanced in a number of ways, they continue to have limitations for flexible profile manufacturing. Incremental forming methods offer potential for flexible profile manufacturing since part geometry is defined primarily by the motions of the forming tools.

The IPF process was invented at TU Dortmund University [1] and allowed the flexible manufacture of tubular structures capable of meeting the challenges mentioned above. The ability of the IPF process to form tubular structures with cross-sectional profiles that vary along their length has been demonstrated [2,3]. However, experimental investigations also indicated that precision of the resulting profile geometry is limited and falls short of the levels expected in industrial production [4]. Unloaded part geometry depends on IPF process response in addition to the machine motions that may be precisely controlled and known. FEM models of process mechanics predict part geometry reasonably well, but their prediction accuracy is not adequate for industrial production [4]. In addition, the computational burden of these models is too high for their effective use in off-line process planning, determination of tool paths, and entirely incompatible with the needs of on-line process control. Therefore, closed loop control of machine motions determined by model-based off-line process planning is inadequate to ensure accuracy of the resulting profile geometry, a fact that is well known for forming operations in general [5].

The goal of the work described here is to formulate a control strategy to improve geometric accuracy of the IPF process by better on-line sensing of process attributes and post-process sensing of product properties of interest, coupled with control-oriented process model development and effective control algorithms. Toward that end, background on the IPF machine and process is provided in Section 2. Improved understanding of process characteristics, obtained from FEM analysis and on-line and post-process sensing of part geometry, is described for the elementary IPF operations of radial indentation (Section 3) and axial grooving (Section 4). Features of IPF relevant to the development of control-oriented models are examined in Section 5 in view of past related work. A control strategy for part geometry, along with directions for future research, is formulated in Section 6, followed by concluding comments in Section 7.

2. IPF process background

The principle of the IPF process is that multiple tools, arranged around the tubular workpiece, move radially into the part and change its cross-sectional geometry locally. Beside radial tool movement for

* Corresponding author.
E-mail address: Srinivasan.3@osu.edu (K. Srinivasan).

https://doi.org/10.1016/j.jmapro.2022.04.034
Received 15 April 2022; Accepted 23 April 2022
Available online 3 May 2022

indenting the tube, axial as well as circumferential motion can be superposed. Fig. 1 shows the process geometry and Fig. 2 shows the IPF machine, with eight servo-controlled axes [2]. It allows parallel utilization of up to six indenting tools capable of radial motion, mounted on a rotary disc for circumferential motion. The eighth degree of servo actuation, not shown in the figure, is a hydraulically actuated cylinder that is clamped to the tube to be profiled. Thus, by implementing appropriate motions of the eight actuators, the indenters can move along arbitrary three-dimensional tool paths in relation to the workpiece, resulting in corresponding flexibility in forming tube cross-sectional profiles and their variation along the tube axis. Single or multiple grooving passes may also be made to generate the desired tube profiles.

Finite element modelling was used by Grzancic [4] to examine the single-pass, single-tool IPF process for radial indentation to 4 mm depth, followed by straight axial grooving for 100 mm and radial tool withdrawal (Fig. 3, tool path). An elastic-plastic material model with isotropic strain hardening was used for the E235 (AISI 1010) steel tube [6], the flow stress σ_f being determined experimentally as

$$\sigma_f = \left(688 - 41.2 \cdot e^{-77.32\varepsilon^{0.725}}\right) \text{MPa} \quad (1)$$

where ε is true strain. Experiments confirmed rate independence of the material model. In computing springback, influence of isotropic strain hardening on material elastic behaviour was not considered [4].

Fig. 3 compares FEM and experimental results for the groove depth trajectory following the completion of the axial grooving. The bulges in the region of radial indentation (start position), as well as the non-uniformity of the groove contour during grooving and tool withdrawal (unloading), are predicted reasonably well by the FEM model, confirming moderately good modelling of the underlying phenomena and understanding of the reasons for geometry error, but indicating the need for improvement in the FEM model also. Importantly, the results indicate that machine control alone is insufficient to ensure adequate product geometry in IPF and motivates the development of additional on-line process and product sensing.

3. Radial indentation — FEM analysis and experiments

Radial indentation is the initial phase of many IPF processes and, owing to its relative simplicity, is a reasonable starting point for validation of models [7] and sensing approaches proposed as part of an overall control strategy. FEM analysis and experimental results will provide insight into the process, as well as indicating the nature of future experimentation. ANSYS Workbench was used for all FEM studies here.

3.1. FEM analysis parameters

Fig. 4(a) shows the Cartesian coordinate system used to describe machine motions as well as the tube deformation field. The longitudinal or axial direction of the tube is the z-axis, and the direction of indentation is along the negative y axis. The origin of the Cartesian coordinate system is at the center of the tube cross-section at the axial location of the tool(s). The positive direction of the z-axis points to the hydraulic actuator moving the tube axially.

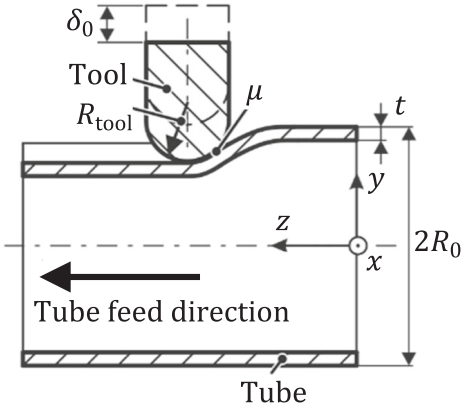

Fig. 1. IPF process geometry [2].

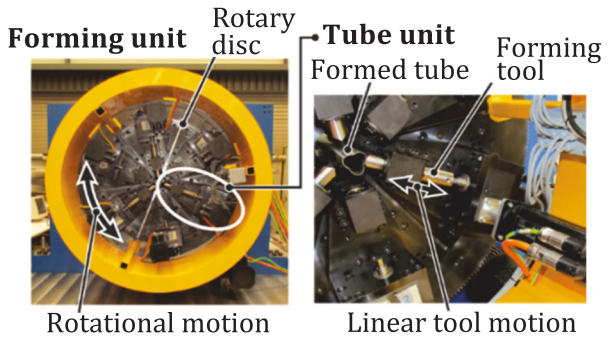

Fig. 2. IPF machine and actuators [2].

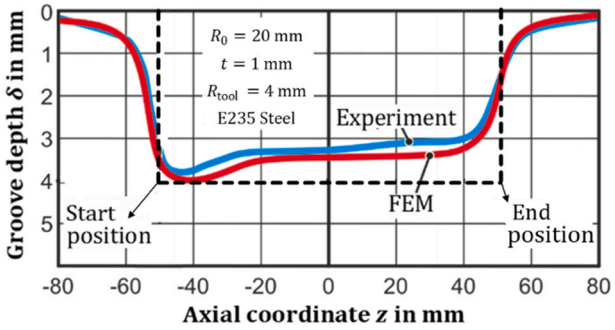

Fig. 3. Unloaded groove depth contour, R_{tool} = 4 mm [4].

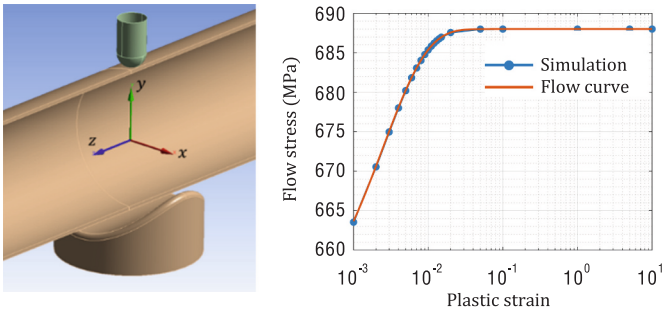

Fig. 4. (a) Radial indentation geometry. (b) Material model approximation.

An indenter with a hemispherical tip shape is shown in the figure and used for simulation and experimental studies, tools with different radii being used for different situations. Other tool geometries were used [8], but corresponding results are not reported here. A crescent shaped support tool with the same diameter as the tube, shown in Fig. 4(a), was used for the single indenter studies reported here. The tube material used in this work is E235 (AISI 1010) steel as in [4], and hence (1) is used for the material model. The tool material used is 42CrMo4 (AISI 4142) steel surface hardened to 60HRC. A piecewise-linear approximation is used for FEM studies, Fig. 4(b) showing the closeness of the approximation to the material model.

Symmetry was used to reduce the computational needs of FEM analysis. Four-fold symmetry was used for indentation with a single indenter and crescent support, and six-fold symmetry was used for radial indentation with three indenters positioned symmetrically around the

circumference of the tube. Hexahedral elements with quadratic shape elements were used, the element length (along tube axis) varying with location, from 0.75 mm × 0.5 mm × $t/3$ (t = tube thickness) at the indenter to 7.5 mm × 0.5 mm × $t/3$ at the end of the tube. Tube support at both ends was simulated as fixed, to maintain the assumed model symmetry, though the tube is clamped at one end and is free at the other end. As in [9], the tube is assumed to be long enough relative to the localized deformation region. Comparison of results obtained with fixed boundary conditions at both ends, and with one side fixed and other side free, resulted in predicted deformation error being significantly less than 0.1 mm. The numbers of nodes and elements for the single indenter simulation were approximately 70,000 and 15,000 respectively and, for the three-indenter case, approximately 110,000 and 25,000 respectively. Other simulation parameters are shown in Table 1. Friction coefficients of 0.3 and 0.075 at the contact surfaces were also simulated, with no noticeable effect on the results.

3.2. Radial indentation analysis — single indenter

FEM analysis indicates that the deformation field due to radial indentation is distributed in space, along both the tube axis and circumference, though the actuation by the indenter is discrete. Understanding of the characteristics of this deformation field will be useful in designing the sensing strategy for effective control.

We focus first on the deformation field in the presence of the indentation load since it is relevant to on-line sensing. Fig. 5 shows the simulated loaded cross-sectional contours, for two axial locations, for the following process conditions in addition to those already specified: $R_{tool} = 4$ mm, $\delta_0 = 6$ mm. The extent of the deformation field around the tube circumference is significant, and tube bulging is evident. Fig. 6 shows the loaded longitudinal contours along the top of the tube ($x = 0$) and indicates that the axial extent of the deformation field is also significant.

At the indenter location, $z = 0$, the imprint of the tool geometry on tube deformation is evident in the contact region (Fig. 5(a)), whereas at $z = 10$ mm, such is not the case (Fig. 5(b)). From these results as well as results for other processing conditions such as tool size, tube size and wall thickness and indentation depths [8], we conclude that there are three broad types of deformed cross-sectional contours in the z direction.

- Zone 1 (low values of z): The tool contact zone. Tool geometry is imprinted on part of the deformed geometry of the tube
- Zone 2 (intermediate values of z): Tool is not in contact with the tube, but its geometry influences the deformed geometry of the tube
- Zone 3 (higher values of z): There is inversion of the cross-section curvature near the top of the tube, and the tube reverts to its undeformed shape at the end of the zone

The deformed tube geometry reflects the nature and magnitude of the stress components and the yielding of the tube under the action of the stress field. The overall pattern of the deformation field in the longitudinal direction shares some features with the 'localized' mode of deformation of a 'pinched' rigid-plastic cylindrical shell [9].

Release of the indenting load results in springback due to partial recovery of elastic deformations. The resulting unloaded cross-sectional and longitudinal contours are also displayed in Figs. 5 and 6, indicating

Table 1
Simulation parameters for radial indentation studies.

Parameters	Value
Young's modulus	1.78×10^5 MPa
Poisson's ratio	0.3
Friction coefficient μ (C)	0.15
Tube outer radius R_0	20 mm
Tube thickness t	1 mm

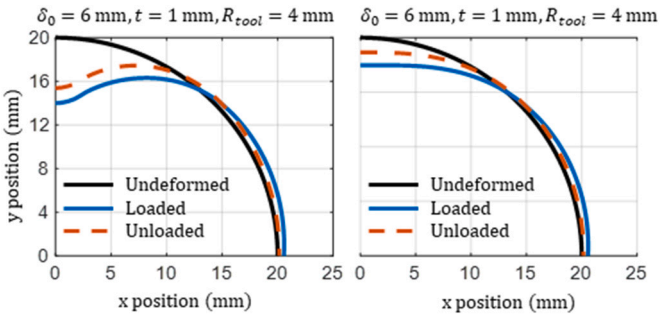

Fig. 5. Simulated cross-sectional contours for (a) $z = 0$ and (b) $z = 10$ mm.

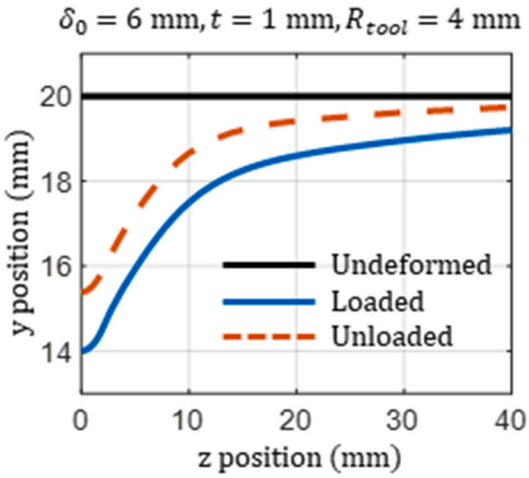

Fig. 6. Simulated longitudinal contours, $x = 0$.

the significance of springback and the need to model this effect to predict final product geometry.

We compute the energy released with the removal of the indenting load as follows. The elastic energy in the tube under loaded conditions is computed using the principal elastic strains. Following the release of the indenting load, residual elastic energy in the tube, associated with the residual stresses, is computed. The difference in the two computed stored elastic energies should show positive correlation with the change in geometry.

The elastic energy stored in the tube under load is given by

$$U = \int dU = \int \frac{1}{2}\{\sigma\}^T\{\varepsilon\}\, dV \tag{2}$$

where dU is the elastic energy in the elemental volume, dV is the volume of the element, $\{\sigma\}$ is the stress vector, and $\{\varepsilon\}$ is the elastic strain vector, both in Voigt notation. The energy is calculated in the three principal directions, and summed to obtain total elastic energy, the process being repeated for loaded and unloaded conditions. The resulting computed energy values are $U_{loaded,elastic}$ and $U_{unloaded,elastic}$ respectively. Total energy storage $U_{loaded,total}$ in the tube in the loaded condition is computed in a similar manner except that total strains are used. The elastic energy recovered is normalized as follows.

$$\left[\frac{\Delta U_{l,el}}{U_{l,tot}}\right] = \frac{U_{loaded,elastic} - U_{unloaded,elastic}}{U_{loaded,total}} \tag{3}$$

This normalized measure of recovered elastic energy is computed for a radial indentation of 6 mm depth and tool radii R_{tool} of 2, 4, and 8 mm, and is seen to grow with tool radius, as shown in Table 2. Fig. 5 shows springback in the cross-sectional contour for the 4 mm tool radius, and Fig. 7 shows results for the other tool radii. Though the figures show

Table 2
Normalized recovered elastic strain energy variation with tool size.

R_{tool} (mm)	Recovered elastic/total strain energy
2	0.1463
4	0.1648
8	0.1714

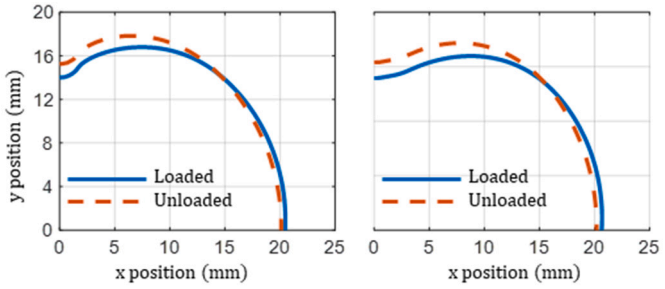

Fig. 7. Cross-section springback for (a) R_{tool}=2 mm and (b) R_{tool}=8 mm.

only a 2D slice of the volumetric effect of springback, they do show that the springback effect also increases with tool radius.

FEM analysis also indicates that part geometry in IPF depends on tool geometry in addition to tool motion, due to the spatially distributed nature of plastic deformation and the fact that part of the deformation field is constrained. Fig. 8 shows loaded cross-sectional and longitudinal contours at $z = 0$ and $x = 0$ respectively for tool radii of 2, 4 and 8 mm and an indentation depth of 6 mm. Clearly, significant regions of the deformation field differ with change of tool geometry. Similar results were seen with other tool geometries [8]. The implication for IPF is that with discrete tool actuation, if the tool geometry and other process conditions are fixed, the achievable profiles, though considerable, cannot be arbitrary.

3.3. Optical sensing of tube deformation

A laser triangulation sensor Micro-Epsilon, Model 2910-50/BL, was used to sense tube deformation on-line during forming, as well as off-line after unloading of the indenter. The sensor was selected due to its sensing capability and size compatibility with the IPF machine. Fig. 9 shows two sensors installed in the machine, and in position to sense the outer surface of the tube. The tube is moved by the hydraulic actuator while the sensors are stationary. The sensors are mounted between indenters, and on the base plate to which the indenting tool holders are attached. One of the indenters is replaced by a crescent shaped tube support for indentation and grooving tests using a single indenter. The laser stripes from the sensors, approximately 50 mm long, show as purple lines and cover the top of the tube as well as the bottom of the tube, to allow tube bending effects to be removed from the measured tube deformation.

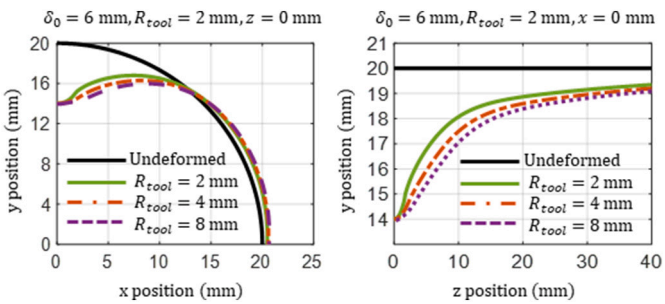

Fig. 8. Loaded contours, $t = 1$ mm. (a) Cross-sectional. (b) Longitudinal.

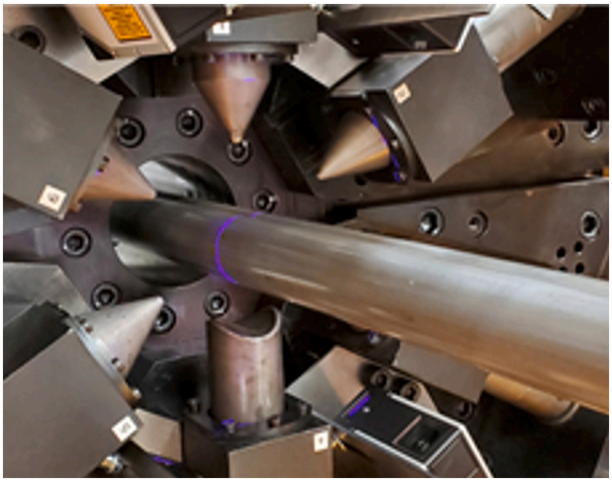

Fig. 9. Optical sensing in position to sense tube cross section on-line.

Fig. 10 shows the steps involved in processing sensor outputs off-line, after a single tube cross-sectional profile is generated, to determine groove depth geometry for an axial groove. The lowest point on each cross-sectional profile is determined to be the groove depth at that axial position. Since the sensors are not integrated with the machine controller, it is assumed that the tube speed is fixed and the same as the programmed tube speed to generate the groove depth profile.

On-line sensing of tube deformation with the sensing system identifies other limitations of the current installation. As is evident from Fig. 9, the indenter bodies themselves limit optical access to the tube outer surface to axial positions no closer than the radius of the indenter bodies, currently 20 mm. Hence, cross-sectional contours measurable on-line are limited to be no closer than 20 mm to the indentation cross-section.

Longitudinal contours are also of interest in describing the deformation field, as is evident from Figs. 6 and 8. The sensor orientation is changed by 90° from that shown in Fig. 9 so that the laser stripe is on the top surface of the tube and aligned with the tube axis, to measure longitudinal contours. Again, the point of the laser stripe closest to the indentation section is limited by the indenter size and may be no closer than approximately 25 mm.

There is thus a need for mechanical and electronic integration of the sensing system with the IPF machine and controller if the sensing capability is to be optimized.

3.4. Radial indentation experiments — single indenter

Loaded and unloaded deformed tube geometry data for radial indentation with a single indenter are compared here with FEM results. The comparison provides insights into possible sources of measurement error, as well as the capabilities and limitations of FEM analysis. Tool radius of 4 mm and indentation depths of 2, 4, and 6 mm were used, other process conditions being the same as for the FEM studies reported earlier. The tube material was E235 steel. Fig. 11 shows the plan view of the tube surface after radial indentation indicating, as did FEM analysis, the spatial extent of the deformation field.

Unloaded cross-sectional contours at the indentation location section ($z = 0$ mm) are compared in Fig. 12 for the three indentation depths noted earlier. The agreement is very good, the difference between the experiment and analysis being within 0.1 mm, and suggests that FEM analysis of the deformation and springback are good. Tube bulging is present in all cases.

Loaded cross-sectional contours are compared for indentation depths of 2, 4 and 6 mm in Fig. 13. The closest axial location for on-line measurement is $z = 20$ mm as noted earlier, and the measured/predicted

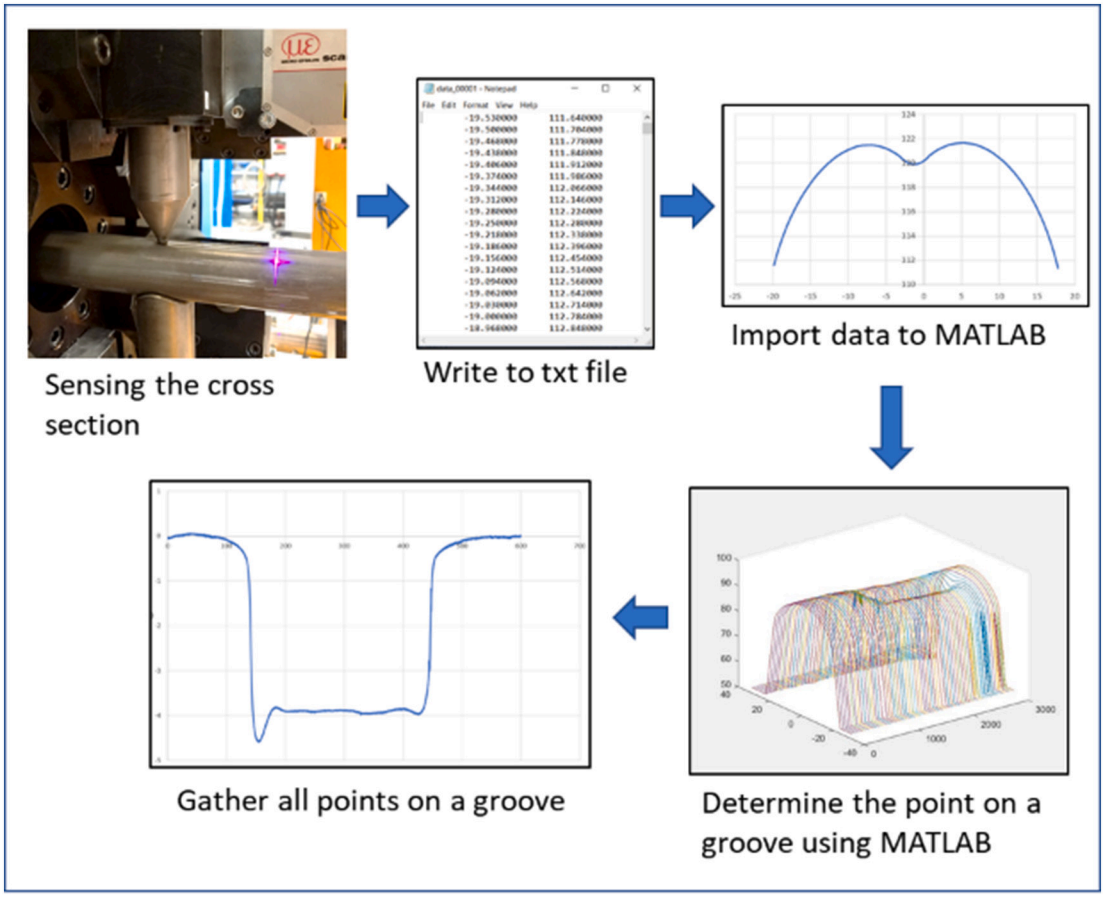

Fig. 10. Off-line sensing of axial groove geometry and data processing.

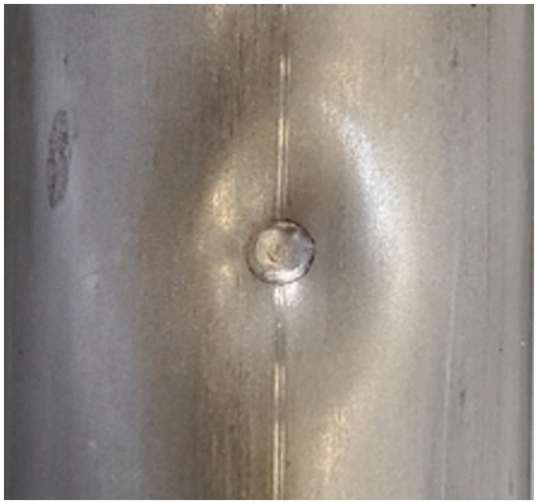

Fig. 11. Plan view of single radial indent.

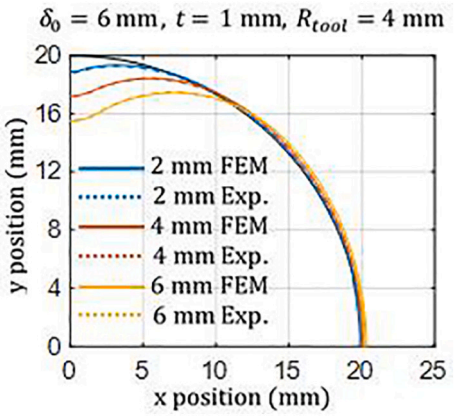

Fig. 12. Unloaded cross-sectional contours, $z = 0$.

deformations are significantly lower as compared to Fig. 12. The difference between prediction and measurement is still within about 0.1 mm. However, given the lower deformation levels, the fractional error is greater than for measurements of unloaded cross-sectional contours, underscoring the penalty resulting from limited optical access. Clearly, on-line measurements that are not so limited are desirable.

Unloaded longitudinal contours along the tube top centreline ($x = 0$) were also measured offline and are compared with FEM predictions in Fig. 14 for the same three indentation depths as in Figs. 12 and 13. Given the lack of direct communication between the sensing system and the IPF controller, axial positions were reconstructed assuming a constant and known tube feed rate. Also, this set of measurements predated the multi-sensor system shown in Fig. 9 for eliminating the effect of tube bending. The zero-deformation location on the tube outer surface was determined visually. Nevertheless, the comparison between measurement and analysis in Fig. 14 is within about 0.2 mm and is good, suggesting again that FEM modelling of springback in radial indentation is good.

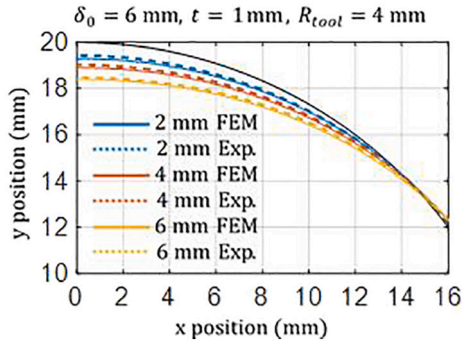

Fig. 13. Loaded cross-sectional contour, $z = 20$ mm.

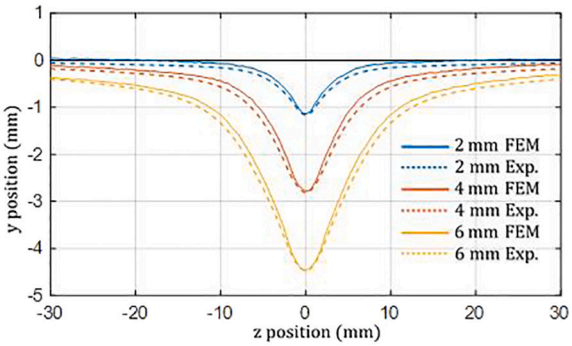

Fig. 14. Unloaded longitudinal contours, $x = 0$.

3.5. Radial indentation analysis — multiple indenters

Deformation and stress fields were determined for radial indentation with multiple indenters using FEM analysis, the deformation field under load being studied in greater detail. The deformation fields are compared here with results for the single indentation case to determine similarities and differences between these cases.

Loaded cross-sectional contours at $z = 0$ were obtained for radial indentation with multiple and single indenters and compared. Three different cases are reported here: a single indenter with a crescent shaped support positioned diametrically across from the indenter, three indenters spaced 120° apart around the tube periphery, and six indenters 60 degrees apart. For all of the cases, hemispherical tools with 4 mm radius and 6 mm indentation depth were used, other process conditions being the same as in Table 1.

Fig. 15 shows the computed loaded cross-sectional contours for all cases at the indentation cross-section ($z = 0$), and Fig. 16 shows computed loaded longitudinal contours of the tube top centerline ($x = 0$). In both cases, the detail on the right of the figures indicates that the extent of the tool contact zone increases with an increase in the number of indenters. More noticeable is the observation, from Fig. 16, that the

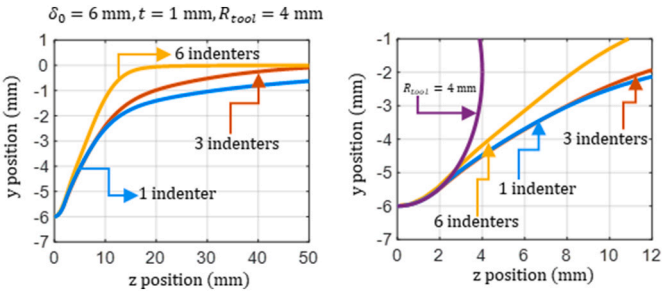

Fig. 16. Loaded longitudinal contour for various indenters, $x = 0$.

longitudinal extent of the deformation zone decreases as the number of indenters increases. The half-axial length of the deformation zone decreases from well over 50 mm for a single indenter to 15 mm for six indenters.

A similar observation of a significant reduction in the axial extent of the plastic deformation zone has been noted by Reid [9] in comparing the deformed region for a pair of opposing lateral loads ("pinched" loads) on a metallic tube and a uniformly distributed lateral ring load around the tube circumference. The loading is clearly non-axisymmetric in the former case and axisymmetric in the latter case. The current observation may be related to the fact that the six-indenter case is closer to axisymmetric lateral loading as compared to the single-indenter or three-indenter case, which are more clearly non-axisymmetric. Reid related the difference in the axial extent of the deformation zone to differences in the dominant components of the stress field. For "pinched" loads, circumferential bending stresses and axial membrane stresses dominate as compared to other stress components. For axisymmetric loads, circumferential membrane stresses and axial bending stresses dominate.

The effect of using multiple indenters on springback in radial indentation is practically relevant as profiles of practical interest would involve multiple indenters. Fig. 17 compares the effect on cross-section springback in radial indentation if three indenters are used instead of one, and Fig. 18 is a zoomed-in comparison. Hemispherical tools with 4 mm radius and 6 mm indentation depth were used in both cases, other process conditions being the same as in Table 1. Springback is lower as the number of indenters is increased, the change in springback being higher than was the case when comparing Figs. 5(a) and 7(a) and (b). Table 3 lists the normalized elastic strain energy recovery using Eqs. (2) and (3). Greater decrease in this metric with increase in the number of indenters is noted in Table 3 as compared to the changes in Table 2, which is in line with the observed larger change in springback in Fig. 17. The springback for radial indentation with six indenters was computed though the result is not displayed and as expected, it was much lower than for the three-indenter case.

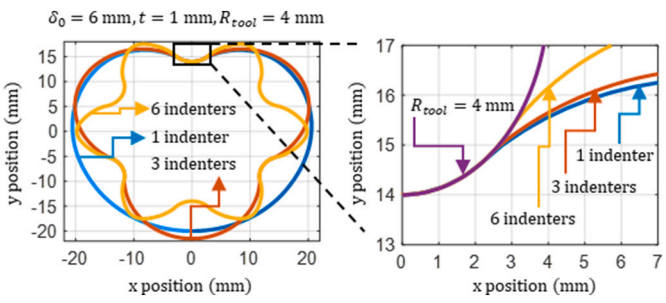

Fig. 15. Loaded cross-sectional contour for various indenters, $z = 0$.

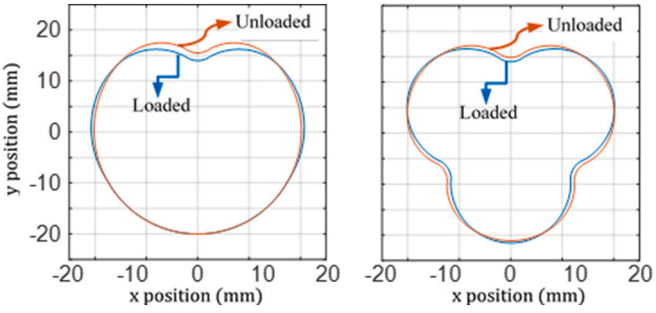

Fig. 17. Cross-section springback at $z = 0$, (a) one and (b) three indenters.

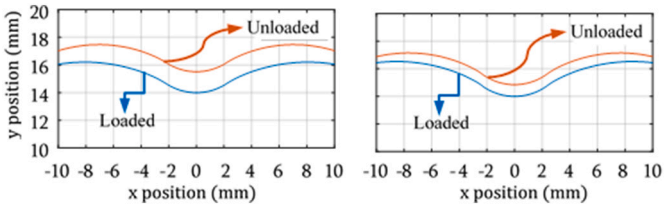

Fig. 18. Cross-section springback (zoomed) at $z = 0$, one and three indenters.

Table 3
Normalized recovered elastic strain energy variation with indenters.

No. of indenters	Recovered elastic/total strain energy
1	0.1648
3	0.0873
6	0.0271

4. Axial grooving — FEM analysis and experiments

Axial grooving is a more representative IPF process than radial indentation as it involves radial/angled indentation at tool entry, axial movement of the tube to create a groove in the tube, followed by tool withdrawal from the tube. This process is therefore more complex to model as it involves more complex temporal changes in the deformation field.

Understanding of axial grooving, and its relationship to radial indentation, will enable future development of control-oriented analytical models of axial grooving. The work described here involves FEM analysis of, and preliminary experiments on, axial grooving with a single indenter.

4.1. Process conditions and FEM analysis methodology

The tube material and material model used are the same as for the radial indentation studies. A single indenter is used with the crescent tool support used for radial indentation. For the indenter, a hemispherical tool with radius of 4 mm was used, and the indentation depth for axial grooving was fixed at 4 mm. All other process conditions are the same as in Table 1.

Two entry/exit trajectories are considered here, involving entry/exit angles of 7.1° and 90° with respect to the tube axis, and a groove length of 200 mm following indentation at constant depth, between completion of the indenter entry and initiation of its withdrawal. Axial tube speed was 4 mm/s. Angled entry and exit are achieved by coordinating radial tool motion with appropriate axial tube motion. The commanded contours for the entry and exit segments with different entry and exit angles are different and bracket the commanded 200 mm long segment of constant groove depth. Comparing these trajectories to that employed by Grzancic [4] and shown in Fig. 3, the trajectories here are intended to examine the effect of changes in entry/exit angles as well as the length of the constant depth segment of the groove trajectory.

The axial grooving setup and boundary conditions are shown along with the specified trajectories, in Fig. 19. The tube is free at one end and fixed at the other end since it is clamped to the hydraulic actuator on the IPF machine. The zero location in the axial direction ($z = 0$) coincides with the start of the 4 mm deep section of the groove.

Two-fold lateral symmetry is used in creating the FEM model for axial grooving, unlike the four-fold symmetry used for the single radial indentation case. Symmetry cannot be used in the axial direction due to the axial movement required for simulating axial grooving. As in the radial indentation case, hexahedral elements with quadratic shape functions were used with sizes varying with location relative to the indenter, from 0.75 mm × 0.5 mm × $t/4$ (t = tube thickness) at the indenter location to 7.5 mm × 0.5 mm × $t/4$ at the end of the tube. These

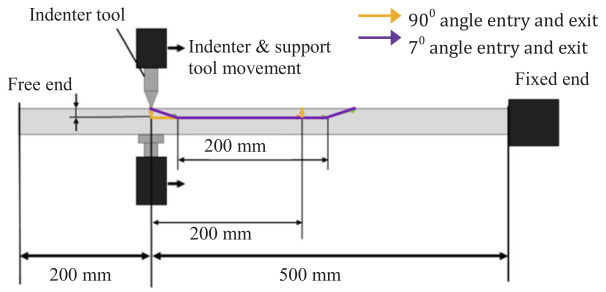

Fig. 19. Axial grooving setup geometry.

element sizes were used for both the trajectories considered here. Other process conditions are the same as in Table 1. The number of nodes was approximately 200,000 and the number of elements approximately 160,000.

4.2. Axial grooving FEM analysis results — single indenter

Deformation and stress fields for axial grooving are computed using the FEM model, as for the radial indentation studies. Unloaded deformations are important for future development of part-to-part process control, and loaded deformations and stress fields are important for future development of on-line process control. Comparison of unloaded and loaded groove geometry between the two trajectories is the focus here, along with comparisons with the single radial indentation case where appropriate. The comparison will highlight the effect of entry and exit angles on groove geometry.

Unloaded longitudinal groove depth trajectories were compared for the two cases. Tube bending upward toward the unsupported end was noted and the groove depth at any axial position determined by taking the difference between the sensed top and bottom displacements. The resulting groove depth trajectories are shown in Fig. 20, zero on the y-axis indicating that the difference between the top and the bottom displacement is same as for the undeformed tube.

Fig. 20 indicates significant differences in groove geometry in the entry and exit regions resulting from differences in the commanded indenter trajectories outside the 0–200 mm range. The groove depth transition region near the end of the groove is seen to be shorter than near the start of the groove. For both trajectories, the groove depth settles to a value of about 4.8 mm after about 50 mm of groove travel at a constant commanded depth. The fact that the steady groove depth is nearly 4.8 mm whereas the commanded groove depth is 4 mm, even in the region of steady axial grooving, is an indication of the complexity of the springback phenomenon in axial grooving.

Comparing these results with those in Fig. 3, we note that when a groove of short enough length is commanded, the region of steady groove depth is apparently absent, the groove depth trajectory being governed by the transients related to entry and exit. Clearly, the complexity of the springback phenomenon in axial grooving poses a

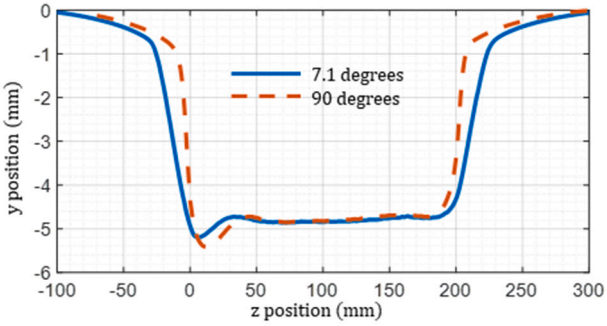

Fig. 20. Unloaded groove depth trajectories for different entry/exit angles.

corresponding challenge for modelling, especially one that is computationally simple.

Unloaded cross-sectional contours at different locations near the beginning and end of the 200 mm long commanded constant depth groove segments (Fig. 19) were computed to see how they evolved with axial location. Fig. 21 shows results for the 90° entry/exit trajectory, the z values on the legends indicating axial location. Fig. 21(a) shows that cross-sectional contour varies significantly with distance z initially, but settles down to a steady contour for values of z greater than about 50 mm. Fig. 21(b) shows cross-sectional contours near the end of the 200 mm long central groove segment, with z values approaching 200 mm. The results indicate, as in Fig. 20, that the transition region near the end of this segment is shorter than near the beginning, with change in the cross-sectional contour from the steady value being small for z values as high as 190 mm. Modelling of the springback phenomenon in axial grooving for the purpose of groove geometry control needs to account for this difference in the unloaded groove geometry in these transitional regions. Cross-sectional contours were computed for the 7.1° entry/exit trajectory as well [8]. They displayed the same trends, the magnitude of the change in the cross-sectional contours being lower.

The relationship of radial indentation to the steady phase of axial grooving is of interest if any analytical and computationally simple model of the former is to be adapted to describe the latter process. The loaded cross-sectional contours at the indenter location for steady axial grooving for the two trajectories were computed using FEM and compared with that for radial indentation, for identical indentation depths and other process conditions, except for the tube speed.

Fig. 22 compares loaded cross-sectional contours at the indenter location in the mid-point of the axial groove (z = 100 mm) for both trajectories as well as for single radial indentation. The contours do not differ perceptibly for the two grooving trajectories, which agrees with the fact that for z = 100 mm the axial grooving process has reached a steady state. Fig. 22 also indicates that the loaded cross-sectional contour for steady axial grooving has significant similarity with that for radial indentation, suggesting that modelling of the loaded geometry for the latter case might well be adaptable to that for the former, adaptation being needed to reduce the difference in the loaded geometry of up to 0.25 mm noted in Fig. 22. While this observation is potentially useful in predicting loaded geometry in axial grooving, it does not address the fact that springback phenomenon in axial grooving seems to be significantly more complex than in radial indentation.

FEM analysis results indicate also that unloaded groove geometry at any axial location evolves with the movement of the indenter, even after the indenter has passed the location of interest, due to the spatially distributed nature of the deformation field and its movement with the indenter location along the tube. This provides motivation to monitor on-line the evolution of the loaded groove geometry with time since such sensing could inform process control action during grooving.

4.3. Axial grooving analysis and experiments — single indenter

Axial grooving tests for the two trajectories described in Fig. 19 were conducted experimentally and the unloaded groove depth trajectories were measured off-line after the conclusion of the tests, using the

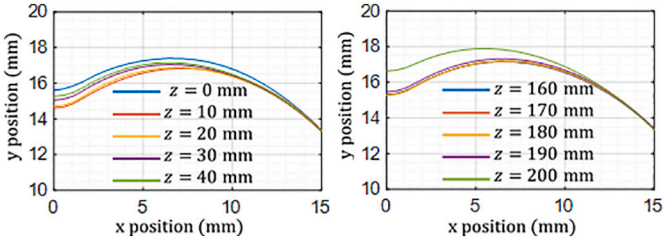

Fig. 21. Unloaded cross-sectional contours at different axial locations.

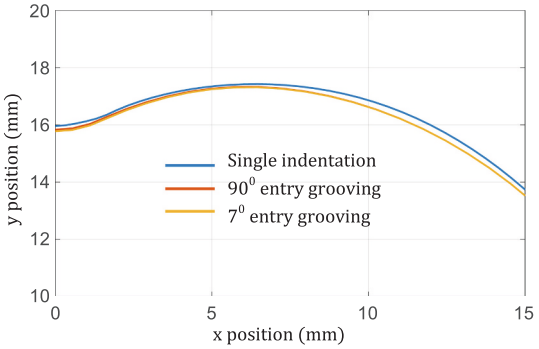

Fig. 22. Loaded cross-section contour: axial grooving and radial indentation.

procedure outlined in Fig. 10. To recreate the unloaded groove depth contours from experiment, unloaded cross-sectional contours at different axial locations were measured. From these cross-sectional contours, the position of the deepest part of the groove was determined and used to reconstruct the groove depth contour.

The results are shown for the trajectory with 90° entry/exit angles and compared with the corresponding FEM analysis result, in Fig. 23. The shapes of the entry and exit groove depth geometries seem to compare well, but there is a difference between FEM and experiment results for groove depths. This difference may be an indication that the unloading and springback phenomena might not be captured well by FEM analysis, or a result of experimental error in generating the groove depth geometry, or a combination of both. The difference between analysis and experiment is greater for the 90° entry/exit case than the 7° entry/exit case [8], suggesting that the modelling of springback in axial grooving is at least partly responsible.

Fig. 24 compares unloaded cross-sectional contours for analysis and experiment at exactly the midpoint (z = 100 mm) in the trajectory corresponding to the 90° entry/exit angles, by which time the grooving process is steady and unaffected by the transition region related to indenter entry. Fig. 24(a) also indicates that the cross-sectional sensors can access the top and bottom of the tube cross-section and can therefore eliminate effects of tube bending. Fig. 24(b) indicates the difference between analysis and experiment varies across the cross-section suggesting again that modelling of springback by FEM is responsible for at least some of this difference.

Fig. 25 shows the on-line sensor configurations and the laser stripe positions and lengths for the sensing system used here, and Fig. 26 describes the locations of the sensor and indenter with respect to the beginning of the central groove segment. S_{dist} is in the range of 20–25 mm for the current sensor installation and T_{dist} varies from 0 to 200 mm. The lateral positioning of the laser stripe in the longitudinal sensing configuration to align it with the tip of the indenter is done visually and is likely to introduce some measurement error.

Fig. 27(a) shows the computed depth trajectories for the axial grooving for different values of T_{dist}, and Fig. 27(b) shows the corresponding measured 50 mm long slices of the depth trajectories sensed in

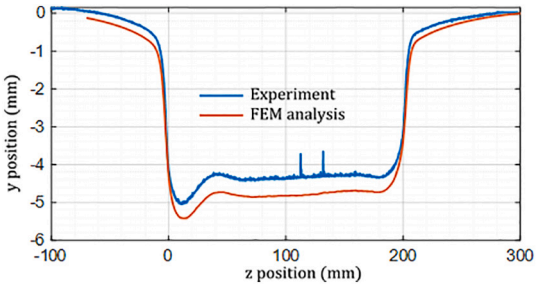

Fig. 23. Groove depth trajectory — FEM analysis and experiment.

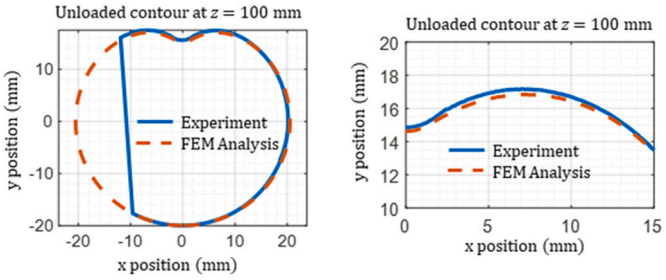

Fig. 24. Unloaded cross-sectional contour — FEM analysis and experiment.

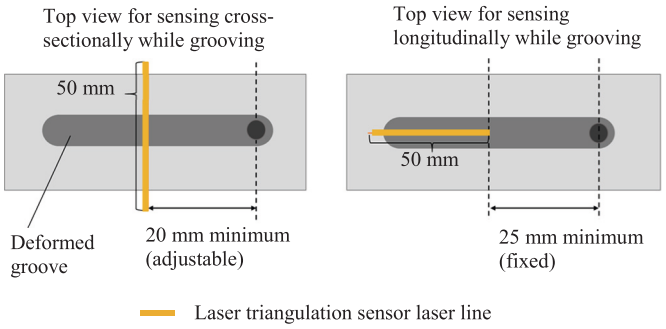

Fig. 25. On-line sensor configurations for axial grooving.

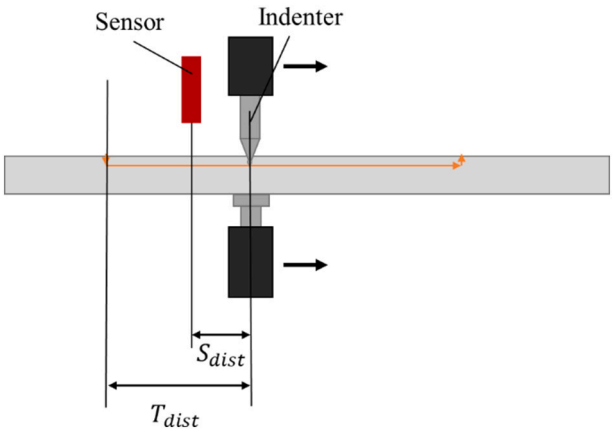

Fig. 26. Sensor and indenter locations for axial grooving experiments.

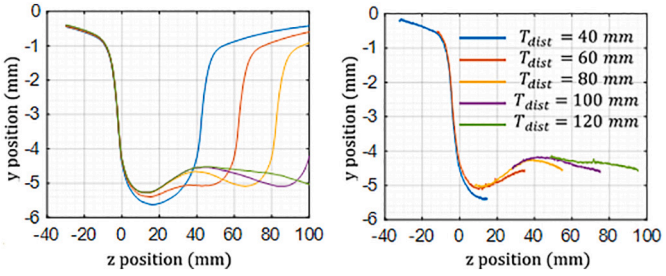

Fig. 27. Partially loaded groove depth trajectories — (a) FEM and (b) experiment.

the longitudinal sensing configuration. As the axial grooving progresses, the indenter moves farther along the groove and the deformation field adjusts to the change in the stresses. Thus, as T_{dist} increases, segments of the previously formed groove recover elastically and the groove depths at corresponding axial locations change, as seen in Fig. 27(a) and (b). The result is that groove geometry is determined by springback that varies with the spatial location of the indenter relative to the groove beginning and, equivalently, with time. Fig. 28 compares groove depth predictions by FEM with measurements and indicates that predicted trends in the on-line groove depth trajectory are confirmed by measurement. The differences noted are believed to reflect a combination of limitations in FEM modelling of springback in axial grooving and measurement error.

5. Control-oriented model development for IPF

The feasibility of on-line measurement of segments of the deformation field in IPF motivates the development of computationally simple models of the process that can form the basis for model-based control design. This category of controllers explicitly incorporates model parameters in controller design and enables controllers to take advantage of model knowledge to effect improved control. The need for computational simplicity arises from the need to simplify the real-time requirements for controller implementation.

Much of the past work on computationally simple analytical modelling of tube deformations under lateral loads was motivated primarily by interest in determining collapse loads for structures. Major assumptions typically made in such work are noted below. Limited research motivated by interest in post-collapse geometry is also summarized.

5.1. Related work on deformation of tubes under lateral loads

Wierzbicki and Suh [10] used a simplified shell model and rigid plastic material characteristics in determining closed form solutions for load vs deformation characteristics of tubular structures subject to lateral loads and large plastic deformations. Loosely connected rings and generators, with compatible lateral deformations, were used to model the mechanics of the tube's deformation during collapse. The axial generators were treated as thin, long beams, exhibiting predominantly membrane action whereas the rings, assumed to be inextensible, exhibited sectional collapse due primarily to circumferential bending. A limited interaction yield surface was assumed, reducing the problem to a set of compatible 1-D problems. Incremental velocity fields for the collapse motions of the rings and generators were specified based on several assumptions. Stationary and moving plastic hinges were used to denote localized yield points of the sectional collapse. Shear and twisting effects were neglected in computing internal energy dissipation. An upper bound method was used to determine the axial extent of the deformed region and the collapse load. The approach correlated well with limited experimental results, and also provided insights into the effect of boundary conditions on the tube's collapse loads.

Morris [11] presented a numerical framework to characterize the lateral deformation of spherical and cylindrical shells to loads applied via a rigid boss, specifically the post-collapse geometry of the deformed region of the shell bounded by the rigid boss and the undeformed regions

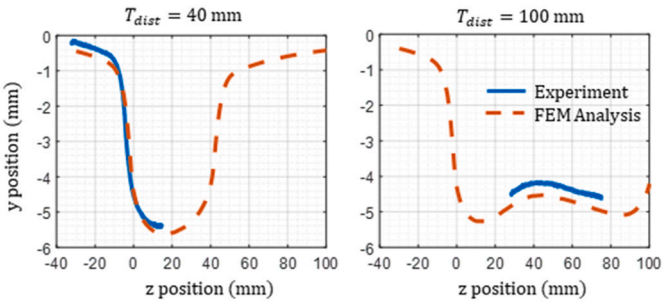

Fig. 28. Comparison of groove depth trajectories — FEM vs. experiment.

of the shell. He also used an upper bound formulation and assumed rigid plastic material behaviour. The more general Ilyushin yield criterion [12] for thin shells was used, the form of the incremental velocity field was specified with the coefficients being unknown, and the generalized strain field was assumed to be related to velocity components using shallow shell theory. Minimization of the internal energy dissipation rate was cast as an unconstrained optimization problem for each small incremental displacement, and the unknown coefficients in the incremental velocity field determined. The deformation of the middle surface of the shell was updated after each increment, and the next increment of displacement was similarly treated. Though reasonable agreement with experimental results for collapse loads was mentioned, verification of the predicted collapse geometry was not reported [11]. Further, this approach to modelling, though less demanding computationally than FEM analysis, is far from being amenable to controller design.

Radial indentation is a reasonable starting point for model development for IPF processes, with a focus on relating indent geometry to indenter motion. Since tube deformation in the tool-tube contact zone is defined largely by the tool geometry, the focus of the model should be on tube deformation outside the contact zone. A computationally simple model for predicting the contact zone boundary, wall thickness reduction and forming forces is available for radial indentation [7]. Correlation of model predictions with FEM analysis and/or experiment is limited.

5.2. Features of the stress field in radial indentation

In developing a model for loaded indent geometry outside the contact zone in radial indentation, the nature of the stress field is relevant since it may allow simplification if some components are negligible [10]. One assumption, evaluated here, is that a plane stress state exists in the circumferential-axial directions or the θ-z plane (Fig. 29), and that normal stresses in the r direction as well as shear stresses in the $r\theta$ and rz planes are negligible. The effect of such a simplification of the stress field on the von Mises stress was examined using FEM analysis results for radial indentation using a single hemispherical tipped indenter, the crescent shaped tool support, and process conditions listed in Table 1. Different tool sizes were considered as well.

The von Mises stress was calculated using Eq. (4)

$$\sigma_v = \sqrt{\frac{1}{2}\left[(\sigma_{rr}-\sigma_{\theta\theta})^2 + (\sigma_{\theta\theta}-\sigma_{zz})^2 + (\sigma_{zz}-\sigma_{rr})^2\right] + 3\left(\tau_{r\theta}^2 + \tau_{rz}^2 + \tau_{\theta z}^2\right)} \tag{4}$$

The corresponding computed stress components at the outer surface of the tube at different axial locations were then compared with the von Mises stress values calculated using the full stress tensor and the corresponding computed stress components. The results indicated that, outside the tool-tube contact zone, a plane stress approximation in the circumferential (θ) - axial (z) curved plane is good. Inside the contact zone, the plane stress approximation is poor [8].

In order to understand the relative significance of stresses along the circumferential and axial directions, stress resultants were calculated. Stress resultants describe resultant forces and moments for shell elements subjected to plane stress by integrating the actions of stress components across the tube thickness, as shown in Eqs. (5)–(7). Resultant forces in the direction i are denoted by N_i, resultant moments are denoted by M_i, where $i = z$ or θ. Shear forces and moments in the ij plane are denoted by Q_{ij} and QM_{ij} respectively, where $i \neq j = z$ or θ. The forces and moments are normalized by $N_o = \sigma_{yield}t$ and $M_o = tN_o/4$ respectively, the fully plastic membrane force and moment at yield for a shell of unit width.

$$\frac{N_i}{N_0} = \frac{1}{\sigma_{yield}t}\int_{-\frac{t}{2}}^{\frac{t}{2}} (\sigma_{ii})d\lambda \tag{5}$$

$$\frac{M_i}{M_0} = \frac{4}{\sigma_{yield}t^2}\int_{-\frac{t}{2}}^{\frac{t}{2}} (\sigma_{ii}\lambda)d\lambda \tag{6}$$

$$\frac{Q_{ij}}{N_0} = \frac{1}{\sigma_{yield}t}\int_{-\frac{t}{2}}^{\frac{t}{2}} (\tau_{ij})d\lambda \tag{7}$$

where λ is the variable of integration and $\sigma_{yield} = 647.2$ MPa is the initial yield stress.

Fig. 30 shows the computed normalized stress resultants for single indentation at three axial locations for axial stretching (N_z/N_0), circumferential stretching (N_θ/N_0), axial bending (M_z/M_0), and circumferential bending (M_θ/M_0), for a tool radius of 8 mm and indentation depth of 6 mm. Normalized stress resultants for shear forces and shear bending are much lower and considered negligible. Other indentation conditions displayed similar stress resultant results [8]. The three axial locations are chosen to represent the three broad categories of cross-sectional deformation in zones 1, 2, and 3 referred to in Section 3.2. The following observations are based on Fig. 30:

- Zone 1 ($z = 0$ mm): Circumferential stretching and axial bending and stretching are dominant at low θ. Axial stretching and

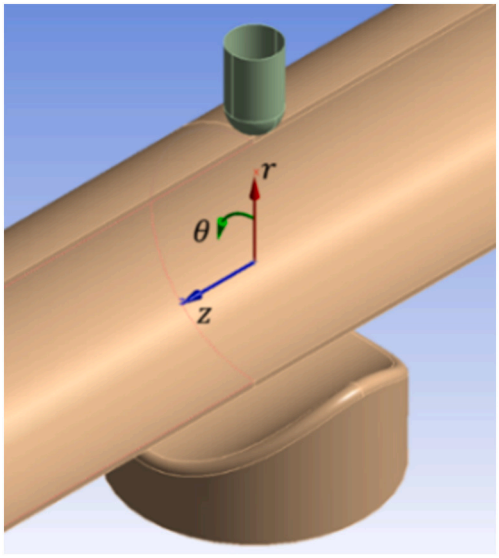

Fig. 29. Cylindrical coordinate system in radial indentation.

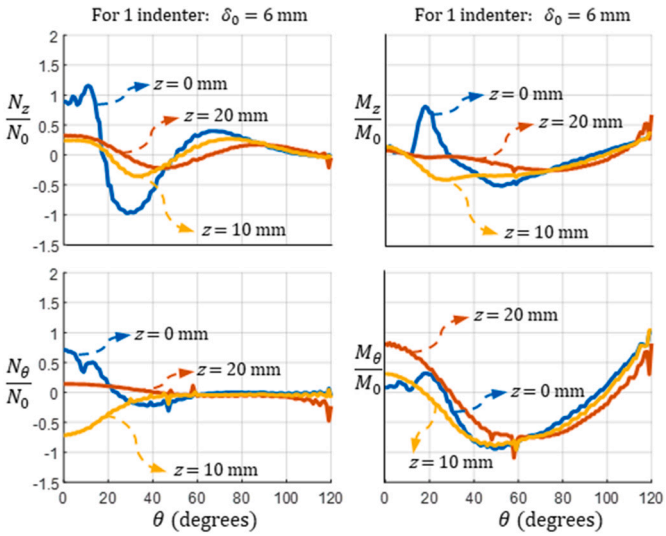

Fig. 30. Normalized stress resultants at three axial locations.

circumferential bending are dominant, and axial bending is significant but much lower, at higher θ.
- Zone 2 ($z \sim 10$ mm): Circumferential stretching is dominant at low θ. Circumferential bending is dominant, and axial bending and stretching are significant but much lower, at higher θ.
- Zone 3 ($z \sim 20$ mm): Circumferential bending is dominant, and axial bending and stretching are significant but much lower, for all θ.

Model development for indent geometry under load may therefore proceed as follows:

- Within the tool-tube contact zone, the indent geometry is determined by the tool geometry. The boundary of the contact zone needs to be determined, along with the boundary conditions for the tube deformation
- Outside the contact zone, the relative significance of the four normalized stress resultants in the three zones along the tube axis may be used to simplify model development.

Pending success in control-oriented model development for radial indentation with a single indenter, refinements of this model to accommodate differences in the stress fields for radial indentation with multiple indenters, and for axial grooving, are warranted.

6. Discussion of the proposed control strategy

Fig. 31 shows the hierarchy of the proposed control strategy for improving geometric accuracy of axial grooving with multiple indenters, an IPF process of practical significance. It is presented here to show the relationship of the work described here to this broader context, and to identify directions for future work needed to realize the goals motivating this research.

While the desired outcome of the process is a specified unloaded profile of known geometry, it needs to be converted into commanded trajectories of the multiple indenters based upon a nominal initial model of the process, process conditions including material model parameters for the tube, and product springback characteristics. The commanded trajectories of the multiple indenters, and the steady tube axial speed, are then programmed as inputs to the machine motion controller. The innermost control loop in Fig. 31 is the machine control loop, and it is the only control loop that is currently implemented in the IPF machine in its stand-alone configuration. The loaded and unloaded tube profile geometry are thus currently generated open loop, with significant error (Fig. 3).

The sensing work described here has established the feasibility of on-line sensing of the cross-sectional and longitudinal contours of the generated profile, under load. Sensing these contours closer to the indentation section is desirable for more effective monitoring of the process and requires better mechanical and electronic integration with the machine. The cross-sectional contour sensed on-line may then be fed back and compared with the desired (nominal) cross-sectional geometry to generate an error measure for the process control loop. The desired (nominal) cross-sectional geometry under load would need to be determined at the outset based upon nominal product springback characteristics, and used as a nominal reference input to the process control loop.

The determination of control action to reduce error in the process control loop effectively requires the design of a model-based controller to reduce trial-and-error in controller design. A computationally simple model for change in the loaded cross-sectional contour in response to change in indenter positions is thus needed. A second need and goal for a process model is to estimate springback characteristics online from the sensed longitudinal contour under load. As noted in Figs. 27 and 28, the sensed longitudinal contour under load contains information on springback. In view of the lack of such models for IPF processes and their complexity as related to processes for which springback is estimated currently [13], modelling for springback estimation will require significant effort.

Estimated springback may then be input to the process controller to update the desired loaded cross-sectional geometry from its nominal value, based upon the in-process estimation of springback. The model-based process controller in Fig. 31 then modifies the commanded trajectories of the multiple indenters based upon the sensed cross-sectional contour and the updated desired cross-sectional geometry.

The development of a process model for use by the process control loop is the goal of ongoing research, whereas the development of a model and procedure for online estimation of springback parameters from longitudinal contour measurements is the goal of future research. The development of the needed models is best when based upon considerations of process mechanics such as those described in Section 5, so that they may be generalized to a variety of process conditions. Empirical determination of process models may offer convenient starting points but needs to be related substantively to process mechanics for greatest utility and value.

While controller design for axial grooving is expected to be relatively straightforward for segments of the axial groove far from the entry and exit transition regions, accommodation of these transitions will require the controller to accommodate time varying model behaviour arising

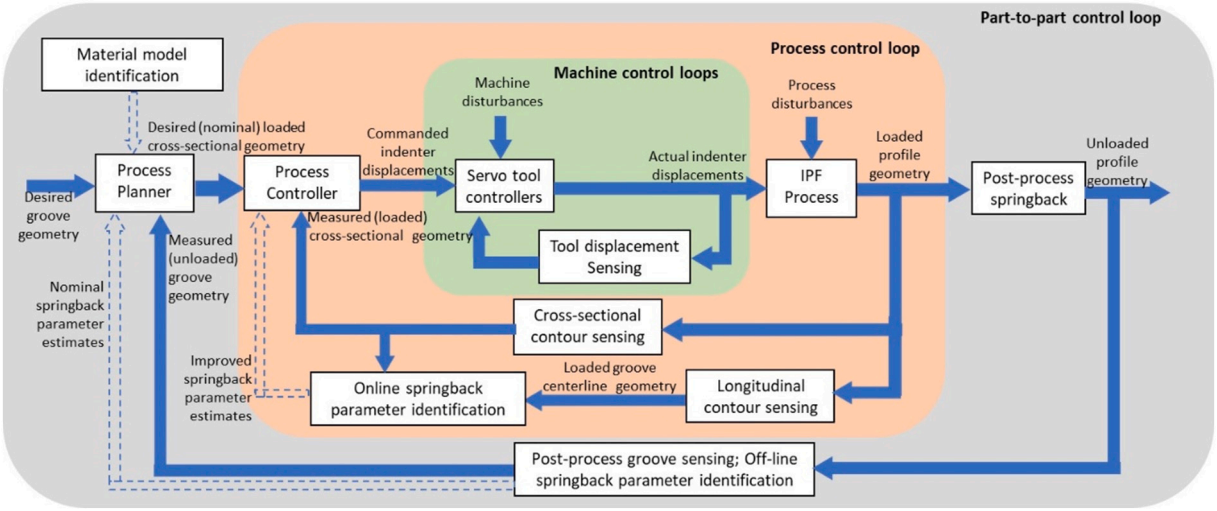

Fig. 31. Proposed control strategy for single pass IPF process.

from the spatially varying relationship of the indenter locations (noted in Fig. 21) to the groove starting and ending locations.

The closing of the process control loop enabled by the developments noted above should improve the geometric accuracy of axial grooving to the extent that on-line estimation of springback and its utilization by the controller is not limited by implementation considerations. However, real-time implementation of the process control is expected to impose some constraints. Off-line sensing of the unloaded axial groove contour and off-line estimation of springback are functions performed with less stringent time constraints. The measured information is also more complete and more likely to be more accurate, as the effects of machine compliance are eliminated. The process planner block, common to other forming operations as well, performs implicit inversion of the overall process model to determine the command for the process control loop, namely, the nominal desired loaded cross-sectional geometry. The material model identification noted in Fig. 31 provides parameters specific to the tube to be grooved, a function that is needed in view of manufacturing variability.

7. Conclusions and recommendations

Improved understanding of incremental profile forming process characteristics is obtained from FEM analysis and on-line and post-process sensing of part geometry in elementary IPF operations. Implications for improvements in on-line sensing of part geometry, control-oriented model development, and controller design are noted, along with appropriate research directions. A control strategy to improve geometric accuracy of the IPF process is presented in the form of a control hierarchy delineating integration of improved sensing, model development and controller design.

Declaration of competing interest

The authors declare that they have no known competing financial interests or personal relationships that could have appeared to influence the work reported in this paper.

Acknowledgements

The work reported here has been supported by National Science Foundation Grant OISE – 1658243, IRES: Forming and Manufacturing Research in Germany. In addition, support of staff in the Institute of Forming Technology and Lightweight Components (IUL), specifically, Eike Hoffmann, at TU Dortmund University is acknowledged.

References

[1] Hermes M, Becker C, Wagner R, Tekkaya AE. Method and device for incrementally shaping profiled pipes, in particular profiled pipes having cross-sections that vary over the longitudinal axis. In: Patent application, WO 2012/000490 A2; 2011. filing date: 06-22.
[2] Grzancic G, Becker C, Hermes M, Tekkaya AE. Innovative machine design for incremental profile forming. Key Eng Mater 2014;622–623:413–9.
[3] Grzancic G, Becker C, Ben Khalifa N. Basic analysis of the incremental profile forming process. J Manuf Sci Eng 2016;138(9):1–6.
[4] Grzancic G. Verfahrensentwicklung und Grundlagen der inkrementellen Profilumformung. TU Dortmund University; 2018. Dr.-Ing.-Dissertation.
[5] Allwood JM, Duncan SR, Cao J, Groche JP, Hirt G, Kinsey B, Kuboki T, Liewald M, Sterzing A, Tekkaya AE. Closed-loop control of product properties in metal forming. CIRP Ann Manuf Technol 2016;65(2):573–96.
[6] Hockett JE, Sherby OD. Large strain deformation of polycrystalline metals at low homologous temperatures. J Mech Phys Solids 1975;23(2).
[7] Grzancic G, Loebbe C, Ben Khalifa N, Tekkaya AE. Analytical prediction of wall thickness reduction and forming forces during the radial indentation process in incremental profile forming. J Mat Proc Tech 2019;267:68–79.
[8] Nakahata R. Analysis, sensing, and analytical modeling of incremental profile forming. The Ohio State University; 2021. MS thesis.
[9] Reid SR. Influence of geometrical parameters on the model of collapse of a "pinched" rigid-plastic cylindrical shell. Int J Sol Str 1978;14:1027–43.
[10] Wierzbicki T, Suh MS. Indentation of tubes under combined loading. Int J Mech Sci 1988;30(34):229–48.
[11] Morris AJ. Non-linear programming for the plastic analysis of local deformations in shell structures. Int J Num Meth Eng 1971;3:215–32.
[12] Ilyushin AA. Plasticité (in French). Paris: Editions Eyrolles; 1956.
[13] Wagoner RH, Wang JF, Li M. In: Springback. ASM handbook metal working. 14B; 2006. p. 733–55.